SCIENCE CHINA
Technological Sciences

•Article•

March 2019 Vol.62 No.3: 406–416
https://doi.org/10.1007/s11431-017-9259-3

Unstable flow characteristics in a pump-turbine simulated by a modified Partially-Averaged Navier-Stokes method

YANG DanDan[1], LUO XianWu[1*], LIU DeMin[2], HUANG RenFang[1] & ZHU ZuChao[3]

[1] *State Key Laboratory of Hydroscience and Engineering, Department of Energy and Power Engineering, Tsinghua University, Beijing 100084, China;*
[2] *Dongfang Electric Machinery Corporation, Deyang 618000, China;*
[3] *Key Laboratory of Fluid Transmission Technology of Zhejiang Province, Zhejiang Sci-Tech University, Hangzhou 310018, China*

Received December 5, 2017; accepted March 16, 2018; published online September 7, 2018

Positive slope characteristics are very important for the safe and stable operation of a pump-turbine. In this study, the unsteady flows in a pump-turbine at pump mode are investigated numerically. To predict the positive slope characteristics with an improved accuracy, a modified Partially-Averaged Navier-Stokes (MPANS) model is employed to capture the unstable physics in a pump-turbine. It is confirmed that the present numerical method predicts the positive slope characteristics in the pump-turbine fairly well compared with the experimental data. It is noted that at the drooping point of the performance curve (positive slope), there are three sets of rotating stall cells in the flow passages of both the guide vanes and stay vanes. In the guide vane region, the flow is completely shut off by the rotating stall, whereas in the stay vane region, the flow passage is partly blocked at the drooping point. The numerical results also reveal that the remarkable variation and high angle of attack (AOA) values upstream the leading edge of the guide vane contribute to the flow separation at the vane suction side and induce rotating stall in the flow passage within the positive slope region. Furthermore, the propagation of the rotating stall is depicted by both Eulerian and Lagrangian viewpoints: the rotating stall blocks the flow passage between two neighboring guide vanes and pushes the flow toward the leading edge of the subsequent guide vane. The rotating stall cell shifts along the rotational direction with a much lower frequency ($0.146f_n$) compared with the runner rotational frequency, f_n.

pump-turbine, positive slope, modified Partially-Averaged Navier-Stokes (MPANS) model, angle of attack (AOA), Lagrangian coherent structure (LCS)

Citation: Yang D D, Luo X W, Liu D M, et al. Unstable flow characteristics in a pump-turbine simulated by a modified Partially-Averaged Navier-Stokes method. Sci China Tech Sci, 2019, 62: 406–416, https://doi.org/10.1007/s11431-017-9259-3

1 Introduction

Pumped storage power plants utilize the excessive electric energy at pump mode and produce energy at the peak load period at turbine mode, which is of tremendous significance for improving the energy efficiency as well as power generation benefit [1]. Because a pump-turbine is the vital component of a pumped storage power plant, it is very important that it is operationally stable and highly efficient. The positive slope phenomenon is a distinct unstable characteristic of a pump-turbine at pump mode under the off-design condition. When a pump-turbine runs in the positive slope region, there is a violent pressure fluctuation and strong noise. Therefore, it is essential to depict the positive slope characteristics of a pump-turbine at pump mode.

The main reason for the positive slope characteristics of traditional centrifugal pumps is the reverse flow at the runner exit [2,3]. However, the internal flow is more complex in a pump-turbine owing to the additional flow part of the guide vanes. Numerous studies have been conducted to investigate

* Corresponding author (email: luoxw@tsinghua.edu.cn)

the unsteady phenomena in a pump-turbine at pump mode by experiment facilities as well as computational fluid dynamics (CFD) methodology. Ciocan et al. [4,5] experimentally investigated the rotor-stator interaction in a pump-turbine via laser Doppler velocimetry (LDV) and particle image velocimetry (PIV) as well as a total pressure survey under different operating conditions. Ran et al. [6] tested the hydraulic performance of a model pump-turbine at pump mode and monitored the pressure fluctuations at typical positions of the flow passage to investigate the unstable characteristics in the positive slope region by experiments. They found that a dominant pressure oscillation component with frequency $0.2f_n$ was induced by the rotating stall in the guide vane region. Lu et al. [7] examined the effect of cavitation on the positive slope region with different guide vane openings in a low-specific speed model pump-turbine experimentally. They pointed out that the variation of cavitation coefficient had a significant effect on the manifestation of rotating stall, but had no obvious effect on the pressure fluctuation frequency induced by the rotating stall. Braun et al. [8] predicted the energy-discharge characteristics with k-ω SST turbulence model and analyzed the detached flow under different conditions. Ran et al. [9] investigated the effect of the rotor-stator interaction on the positive slope characteristics using Spalart-Allmaras turbulence model. The runner was optimized by modifying the blade exit angle and warp angle based on the flow analysis. Liu et al. [10] employed an improved cavitation model to predict the internal flow and pressure fluctuations in a pump-turbine. They stated that the simulation using the mixture model achieved a closer result to experimental data compared with a single-phase model. Pressure fluctuations of a pump-turbine at pump mode were also investigated by Sun et al. [11,12], Guo et al. [13], and Pacot [14].

Though a few of researchers have investigated the positive slope phenomenon in pump-turbines, the unstable turbulent flow and its evolution should be understood for the future development of pumped storage technology. In the present work, a newly developed turbulence model, i.e., a modified Partially-Averaged Navier-Stokes (MPANS) model is used to study the instability characteristics in the positive slope region of a high-head pump-turbine at pump mode. The unsteady flows in the pump-turbine are also simulated by the k-ω SST turbulence model for comparison. The internal flows are carefully analyzed at three operating points to investigate the mechanism of the rotating stall propagation near the drooping point by both Eulerian and Lagrangian viewpoints.

2 High-head pump-turbine

This study considers a high-head pump-turbine having a specific speed of 23.5 $\text{min}^{-1}\ \text{m}^3\ \text{s}^{-1}\ \text{m}^{-1}$. Figure 1 shows the calculation domain of the pump-turbine model, whose flow passage is comprised of spiral casing, stay vane, guide vane, runner and draft tube. In this study, the guide vane opening is set as 13°. The specifications of the pump-turbine at pump mode are listed in Table 1.

3 Numerical methods

3.1 Governing equations

The continuity and momentum conservation equations for the unsteady flow can be expressed in the Cartesian coordinates as eqs. (1) and (2)

$$\frac{\partial \rho}{\partial t}+\frac{\partial(\rho u_j)}{\partial x_j}=0, \tag{1}$$

$$\frac{\partial(\rho u_i)}{\partial t}+\frac{\partial(\rho u_i u_j)}{\partial x_j} = -\frac{\partial p}{\partial x_j}+\frac{\partial}{\partial x_j}\left[(\mu+\mu_t)\left(\frac{\partial u_i}{\partial x_j}+\frac{\partial u_j}{\partial x_i}\right)\right], \tag{2}$$

where u_i is the velocity in the i-th direction, p is the pressure, ρ is the density, μ is the laminar viscosity, and μ_t is the turbulence viscosity.

Because the unstable flow in the positive slope region is extremely complex, turbulence model demands careful consideration to precisely include the flow separation in the pump-turbine. Girimaji [15] proposed the PANS method that

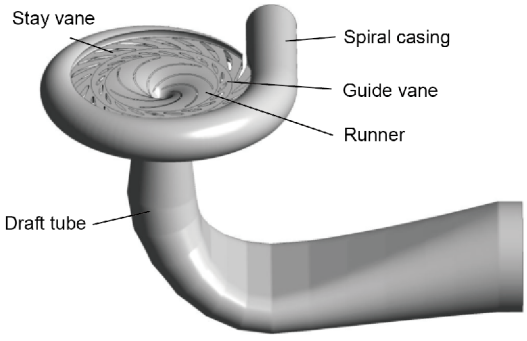

Figure 1 Computational domain of the pump-turbine.

Table 1 Specifications of the pump-turbine at pump mode

Parameter	Value
Runner outlet diameter D_2	547 mm
Runner inlet diameter D_1	250 mm
Runner blade number Z	7
Stay vane number Z_s	20
Guide vane number Z_g	20
Height of guide vane b_0	37.75 mm
Runner rotational speed n	1100 r min^{-1}

varied from the Reynolds-Averaged Navier-Stokes (RANS) to direct numerical simulation (DNS) through two filter-control parameters, i.e., the unresolved-to-total ratios of kinetic energy f_k and dissipation f_ε, which are defined in eq. (3).

$$f_k = \frac{k_u}{k},\ f_\varepsilon = \frac{\varepsilon_u}{\varepsilon}. \tag{3}$$

Because the distribution of f_k depends on the model geometry and physical effects, a MPANS model was improved in refs. [16,17]. They modified f_k as a function of the physical grid ($\delta=(\delta x\times\delta y\times\delta z)^{1/3}$) and local turbulence length scale ($l=k^{1.5}/\varepsilon$), and defined as

$$f_k = \min(1, 3(\delta / l)^{2/3}). \tag{4}$$

The turbulence governing equation in the MPANS model treats the standard k-ε turbulence model as the parent RANS model as expressed in eqs. (5) and (6):

$$\frac{\partial(\rho k_u)}{\partial t} + \frac{\partial\left(\rho u_j k_u\right)}{\partial x_j} = \frac{\partial}{\partial x_j}\left[\left(\mu + \frac{\mu_t}{\sigma_{ku}}\right)\frac{\partial k_u}{\partial x_j}\right] + G_{k\,u} - \rho\varepsilon_u, \tag{5}$$

$$\frac{\partial(\rho\varepsilon_u)}{\partial t} + \frac{\partial(\rho u_j \varepsilon_u)}{\partial x_j} = \frac{\partial}{\partial x_j}\left[\left(\mu + \frac{\mu_t}{\sigma_{\varepsilon u}}\right)\frac{\partial \varepsilon_u}{\partial x_j}\right] + \frac{C_{1\varepsilon}\varepsilon_u}{k_u}G_{ku} - C^*_{2\varepsilon}\rho\frac{\varepsilon_u^2}{k_u}, \tag{6}$$

where G_{ku} is the unresolved production term, and unresolved kinetic energy σ_{ku}, dissipation Prandtl numbers $\sigma_{\varepsilon u}$, and the value of $C^*_{2\varepsilon}$ are defined by

$$\sigma_{ku} = \sigma_k\frac{f_k^2}{f_\varepsilon},\ \sigma_{\varepsilon u} = \sigma_\varepsilon\frac{f_k^2}{f_\varepsilon},\ C^*_{2\varepsilon} = C_{1\varepsilon} + \frac{f_k}{f_\varepsilon}(C_{2\varepsilon} - C_{1\varepsilon}). \tag{7}$$

The turbulence viscosity of the MPANS model is described as

$$\mu_t = C_\mu\frac{k_u^2}{\varepsilon_u},\ C_\mu = 0.09. \tag{8}$$

3.2 Mesh generation

A structured mesh is generated for each part of the pump-turbine as shown in Figure 2. The mesh near the walls of the guide vane and runner is carefully refined to satisfy the requirement of the y^+ value, and its details are also shown in the figure. For the MPANS turbulence model, the y^+ value of the wall-adjacent cells should range from 30 to 300. The y^+ values of the runner blade, stay vane, and guide vane are listed in Table 2.

Four sets of meshes with different element numbers are generated for the mesh independence test in the pump-turbine model. Figure 3 illustrates the comparison of the calculated head coefficient ψ and hydraulic efficiency η with different mesh numbers at the best efficiency point. The head coefficient is defined as

$$\psi = \frac{2gH}{\omega^2 R_1^2}, \tag{9}$$

where g is the acceleration of gravity, H is the head of the pump-turbine, ω is the rotating speed of the runner, and R_1 is the radius of the inlet of the runner (at pump mode).

The mesh number is increased from 1.2×10^6 to 4.2×10^6. Note that when the mesh element number is larger than 3.2×10^6, the head coefficient and hydraulic efficiency of the pump-turbine remain unchanged. Therefore, the mesh with 3.2×10^6 elements is employed as the final mesh scheme in the following simulations in consideration of the computational resource and numerical accuracy.

Table 2 Mesh y^+ information

Component	Minimum	Maximum	Average
Runner blade	8.87	336.54	96.69
Stay vane	1.63	127.87	35.90
Guide vane	2.34	160.44	53.28

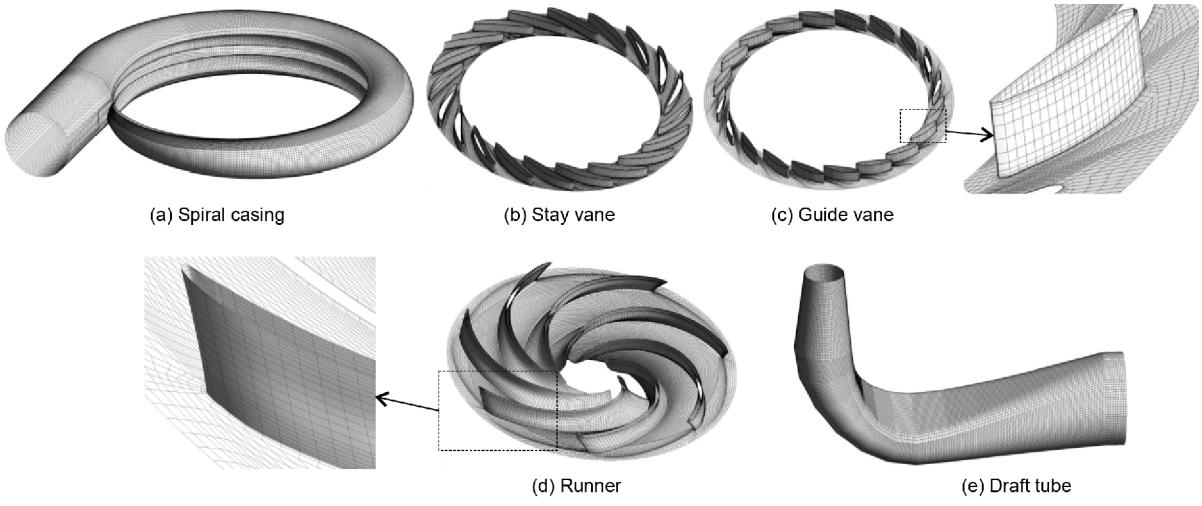

Figure 2 Mesh generation of each flow component.

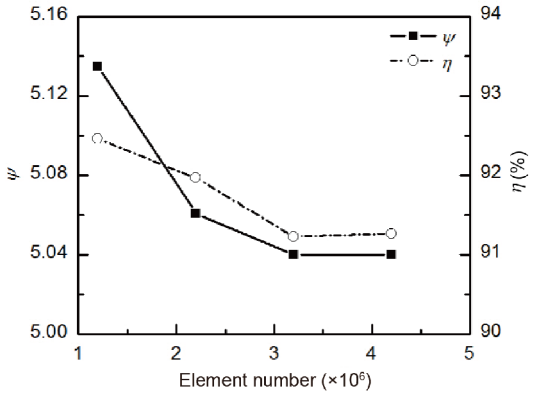

Figure 3 Mesh independence test.

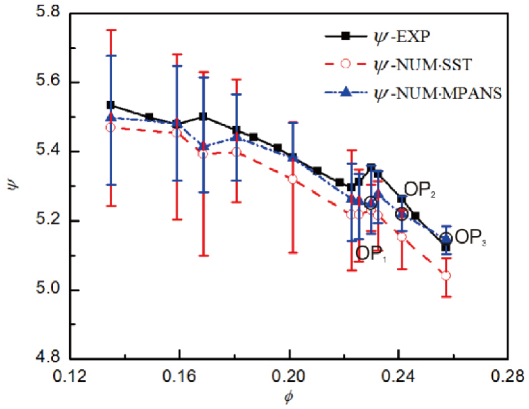

Figure 4 (Color online) Characteristic curves near the positive slope.

3.3 Boundary conditions

The mass flow rate is assigned at the draft tube inlet based on the experiment data. At the outlet of spiral casing, the static pressure (p=100 kPa) is specified for all the cases without cavitation. A rotating frame is applied for the runner zone, whereas the other regions are in a stationary frame. The interfaces between the runner zone and neighboring stationary flow components are set as transient rotor-stator model. Non-slip wall condition is set for the solid surfaces.

CFD commercial code CFX is applied for the numerical simulation. As a basic calculation 6°/time step is considered for 500 steps, and then 2°/time step is used in the subsequent unsteady simulation for a better accuracy. High resolution scheme is set for the advection term.

4 Results and discussion

4.1 Positive slope characteristics

The experimental measurements were conducted at the DF150 hydraulic test rig of Dongfang Electric Corporation (DEC), China. The mass flow coefficient is defined as

$$\phi = \frac{Q_m}{\pi\omega\rho R_1^3}, \tag{10}$$

where Q_m is the mass flow rate.

The characteristic curves near positive slope by different turbulence models are compared with the experimental data in Figure 4. In the figure, "EXP" represents the experimental data, and "NUM·SST" and "NUM·MPANS" indicate the numerical data predicted by the k-ω SST turbulence model and MPANS model, respectively. The vertical bar indicates the variation over the average value for each calculation point. Overall, both the turbulence models predict the head-flow discharge relation in good agreement with the experimental data. Due to the unsteady flow feature of the pump-turbine, there is an oscillation of head coefficient at each operation condition. We can see that the oscillations are small in the large flow rate region, but they become stronger in the drooping zone and under the part flow conditions. For the k-ω SST turbulence model, the head coefficient discrepancies between the predicted mean values and experimental data are less than 3% for all the operation conditions. The head coefficient deviation from the corresponding experimental value is less than 4% in the large flow rate region, but 8% under the operation condition of positive slope. For the MPANS turbulence model, the head coefficient discrepancies between the numerical mean values and experimental data are less than 2%. The head coefficient deviation from the corresponding experimental value is less than 2% in the large flow rate region. The results indicate that MPANS model yields more accurate numerical result than the conventional k-ω SST turbulence model for the pump-turbine. Therefore, we applied the MPANS turbulence model in this paper to investigate the internal flow and depict the physics of the flow near the positive slope with detailed flow information.

4.2 Internal flow analysis

Three operating points on the characteristic curve are selected to analyze the internal flow of the pump-turbine, which are marked in Figure 4. Note that OP_1 represents the operating condition at the first drooping point at pump mode, OP_2 represents the larger flow rate point and OP_3 represents the best efficiency point.

Figure 5 displays the streamline and static pressure distributions on the mid-span section of the runner at different operating points. At best efficiency point OP_3, the flow is smooth in each blade-to-blade passage, though there seems to be slight flow separation along the pressure side of the runner blade. The pressure distribution is similar for each blade-to-blade passage in the runner. With decreasing flow coefficient, the flow separation near the pressure side of the blade aggravates at OP_2, and there occurs a non-uniform pressure distribution at the runner exit. When the flow

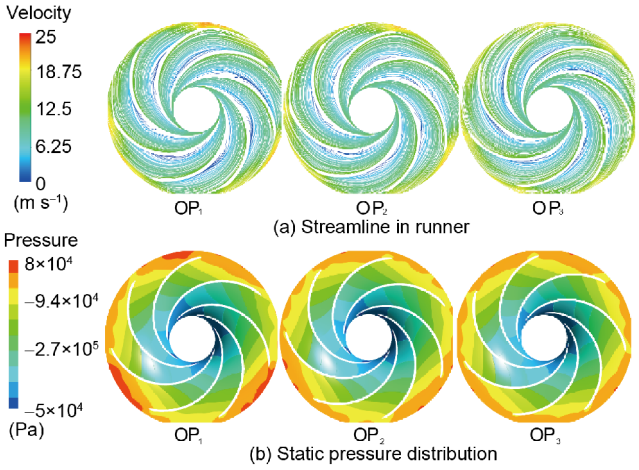

Figure 5 (Color online) Streamline and static pressure distributions on the blade mid-span surface at different operating points.

coefficient reaches drooping point OP_1, obvious flow separation can be seen near the blade pressure side. It is noted that the pressure distribution is uneven at the runner exit compared with the other two operating points. There are three zones with high pressure at the runner exit.

Streamline distributions on the mid-span surface of guide vane, stay vane, and the spiral casing at different operating points are shown in Figure 6. At best efficiency point OP_3, the flow is uniform in the flow passage, except there is slight flow separation near the tongue of the spiral casing. At OP_2, the separation near the tongue of the spiral casing expands, and there is flow separation at the trailing edge of three sets of guide vanes marked in the figure. At drooping point OP_1, the separation near the spiral casing tongue further develops to the next stay vane passages. There are still three sets of flow separation in the guide vane passage. For each set, there are two separation areas linking the suction side trailing edge of the guide vane and the pressure side leading edge of the subsequent guide vane. At the downstream, there are two separation areas in the neighboring flow passages of stay vane corresponding to the flow separations in the guide vane flow passage. Furthermore, it is also clear that the flow separation in the stay vane can interact with the spiral casing tongue and cause a remarkable flow blockage in the stay vane near the tongue.

Figure 7 presents the distribution of swirling strength in a circular section at three operating points. Note that the section is a cylinder having a diameter of $1.15D_2$. Swirling strength λ_{ci} is defined as the imaginary part of complex eigenvalue of the local velocity gradient tensor, representing the strength of the local swirling motion and identifying the shear motions and vortices. As shown in Figure 7(a), the distribution of swirling strength is relatively uniform in each guide vane passage at best efficiency point OP_3. With the decreasing flow coefficient, the magnitude of swirling strength increases and the distribution of swirling strength

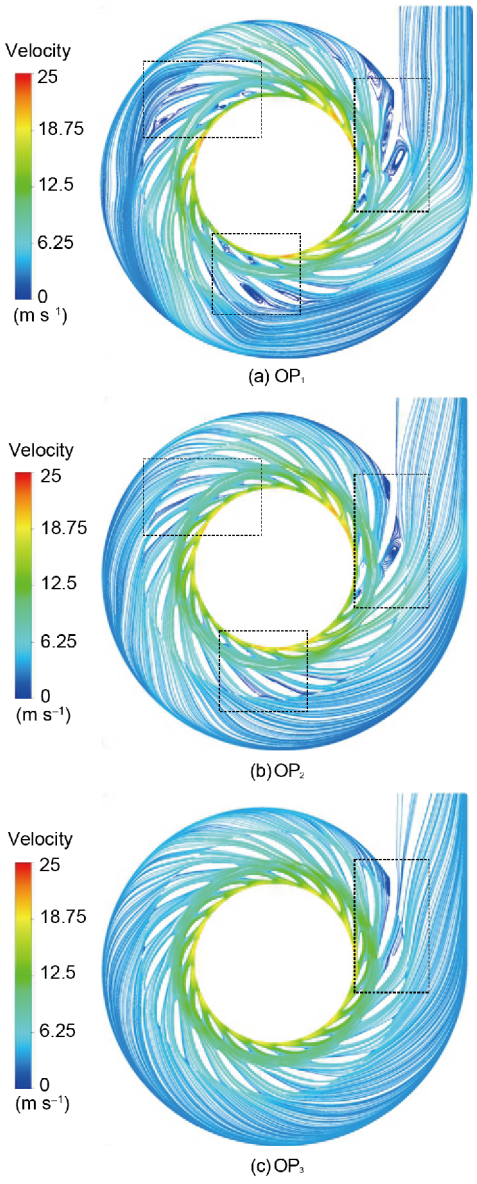

Figure 6 (Color online) Streamlines on the mid-span surface at different operating points.

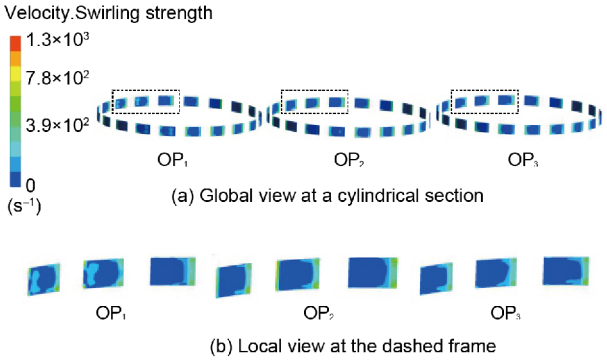

Figure 7 (Color online) Swirling strength distribution at different operating points.

becomes uneven in each flow channel. Local enlarged views of three flow passages between two neighboring guide vanes

are shown in Figure 7(b). At OP_3, there are hardly intensive vortexes in the flow passage between two neighboring guide vanes, except the area near the guide vane walls. However, at drooping point OP_1, intensive swirling strength is observed in the passage between the guide vanes, where the flow separates as shown in Figure 6. It indicates that there are strong vortex motions at drooping point OP_1 compared with the other two operation conditions.

4.3 Angle of attack

For better understanding of flow behavior, the angle of attack (AOA) is discussed to explain the flow separation in the pump-turbine. Note that the flow angle is calculated using the direction of the absolute flow upstream of a guide vane based on the simulation result, and AOA is defined as the difference between the setting angle of guide vane and flow angle. Figure 8 illustrates the distributions of AOA at the leading edge of guide vane on the mid-span at different operating points. It is remarkable that the flow exhibits significant AOA variation owing to the presence of the guide vane. The AOA distribution ranges from −8° to 8° at best efficiency point OP_3. The distribution of AOA presents a periodic variation owing to the interaction between the runner blade and guide vane. At OP_2, because the effect of the runner blade-guide vane interaction is obvious, there are several peaks with larger incidence. At OP_1, three sets of AOA peaks occur for one revolution. For each set, there are two pulses, with the higher pulse being larger than 20°. This large incidence will cause strong flow separation near the suction side at the guide vane leading edge. In the same figure, three pulses with AOA between −8° and −10°, which may result in flow separation near the pressure side of guide vane, can be found at OP_1. These features for AOA distribution indicate the flow separation mainly occurs at the suction side of guide vane. Concurrently, the separation may occur near the pressure side of the other guide vanes.

Figure 9 exhibits the AOA and flow angle (α) distributions along two lines in the vaneless region at drooping point OP_1. For convenience, several guide vanes are marked as A to E. Line 1 is an arc segment of the circumferential line (guide vane mid-span, radial position of $1.095D_2$) with θ ranging from 70° to 120° in accordance with Figure 8, and located just upstream the guide vane. The velocity vector is also displayed in Figure 9(a). Along Line 1, at θ of approximately 85°, corresponding to the leading edge position of guide vane B, AOA reaches the maximum value of 18° and there is flow separation near the center of this vane as shown in Figure 9 (a). At θ of approximately 103°, corresponding to the leading edge of guide vane C, AOA reaches another peak having 15°, and flow separation is expected to occur. After the above two AOA peaks, at θ of approximately 115°, corresponding to the position near the suction side center of guide vane C, AOA

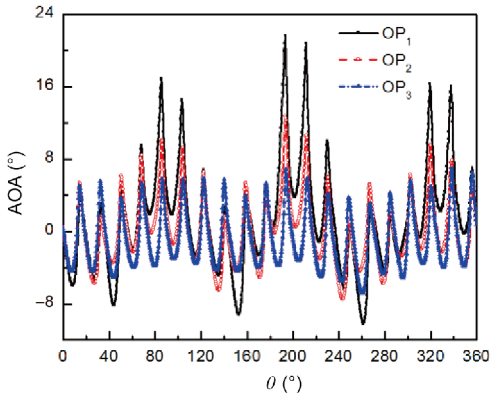

Figure 8 (Color online) AOA distributions at different operating points.

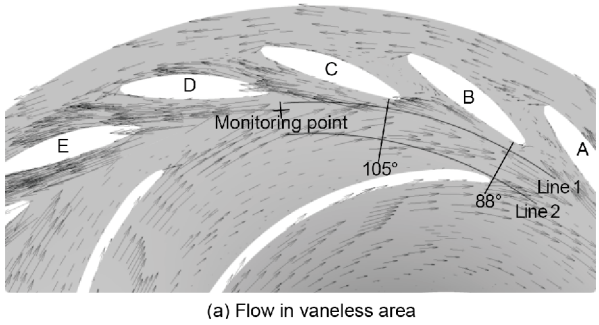

(a) Flow in vaneless area

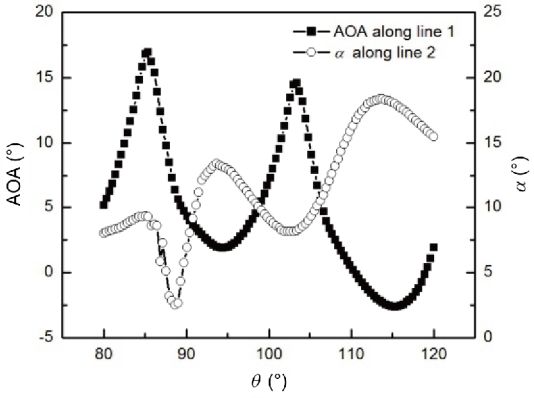

(b) AOA and α distributions

Figure 9 Flow and AOA/α distribution in the vaneless region at OP_1.

reaches the minimum value of less than −3°. The negative AOA implies the flow impingement against the suction side of guide vane C. The results shown in Figures 6, 7, and 9 indicate that the flow with large incidence angles near the leading edge of guide vane B and C results in flow separation from the center of the vane suction side and blocks the flow passages between guide vane B and C and guide vane C and D. Therefore, the flow in vaneless area is pushed through the flow passage between guide vane D and E, and a "jet" can be seen in Figure 9(a).

Line 2 is an arc segment of the circumferential line (runner blade mid-span, radial position of $1.01D_2$) with θ ranging

from 70° to 120°, and is located downstream the runner exit. The flow angle distribution along Line 2 indicates that the flow downstream the runner exit is non-uniform at drooping point OP_1. At θ of approximately 86°, α suddenly decreases, and the flow angle becomes very small. The small flow angle corresponds to the large incidence at the leading edge of guide vane B, at θ approximately 85° along Line 1. At θ of approximately 88°, α further decreases to the minimum value of 2.5°, which is due to the dual effect of the passage blockage of the guide vane and runner wake. It is evident that the obvious variation of flow direction due to the interaction between the runner blade exit and guide vane leading edge contributes to the flow separation in the flow passage between the guide vanes and results in the distinct characteristic curve with positive slope for the pump-turbine.

4.4 Propagation of rotating stall cells

According to our previous study, the flow phenomena such as the flow separation at the passage between guide vanes B and C, and the "jet" between guide vanes D and E are called rotating stall in the pump-turbine at pump mode. According to the results shown in Figures 5–8, there are three sets of rotating stall cells in the entire flow passage. For better understanding, Figure 10 shows the streamlines on the mid-span section during two runner revolutions at drooping point OP_1. In the figure, the color legend shows the velocity magnitude. The behavior of one set of rotating stall is analyzed in the region including guide vane and stay vane. Several stay vanes are marked as A′ to E′, respectively.

At the instant of $t=T/6$, there is a set of clearly rotating stall cells in the flow passages between guide vanes A and B, and guide vanes B and C. Concurrently, a slight flow separation occurs at the suction side trailing edge of guide vane C. In the corresponding downstream stay vane channels, a set of rotating stall cells are observed in the flow channels between stay vane A′ and B′, and between stay vane B′ and C′. Furthermore, there is a "jet" with high speed in the flow passage between guide vane D and E.

From $t=2T/6$ to $5T/6$, the rotating stall moves counterclockwise. The flow separation in the flow channel between guide vanes C and D develops, whereas that between guide vanes A and B is limited at the suction side trailing edge of guide vane A. Correspondingly, the flow separation in the flow passage between stay vanes B′ and C′ enhances, and that between stay vanes A′ and B′ disappears gradually.

From $t=T$ to $9T/6$, the flow separation begins at the suction side trailing edge of guide vane D, and expands to the entire

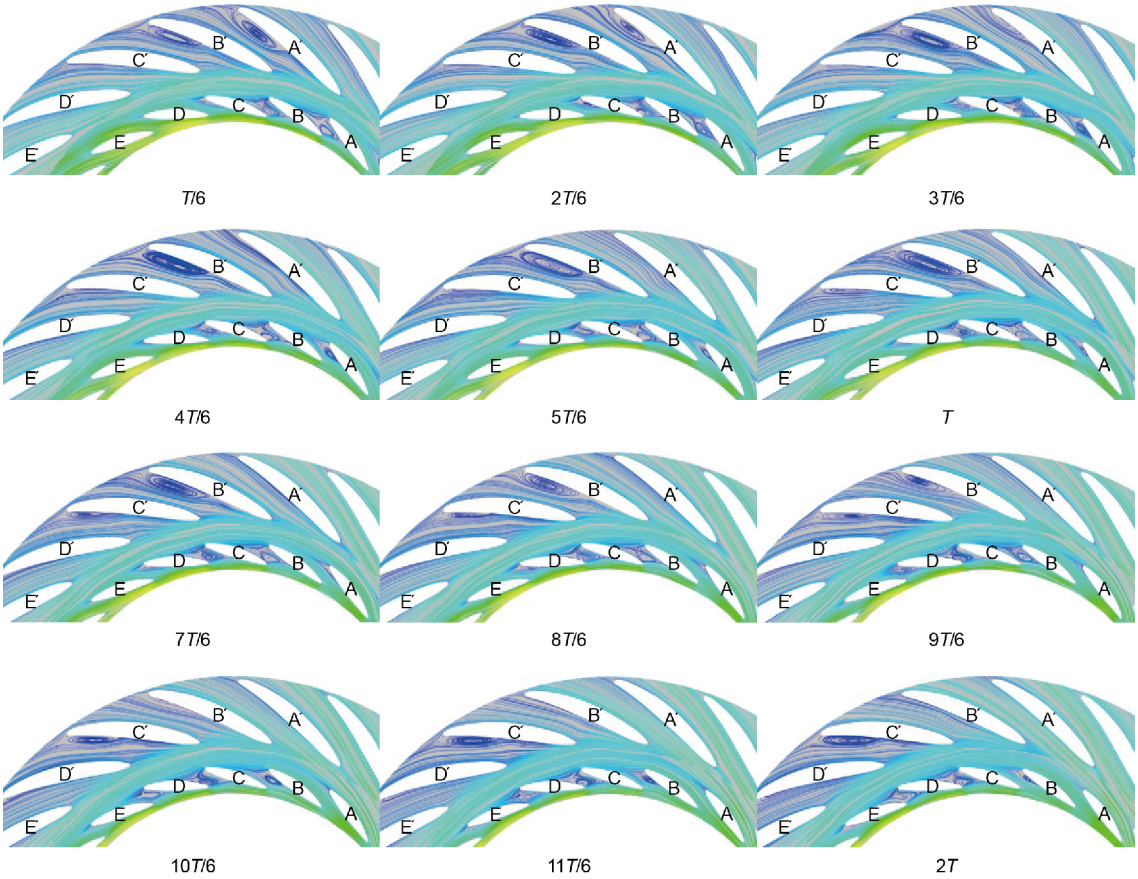

Figure 10 (Color online) Streamlines on the mid-span during two runner revolutions at OP_1.

flow passage between guide vanes D and E. At the downstream in the stay vane region, the flow separates near the suction side trailing edge of stay vane C′ at $t=T$, and the separation develops from then on. From $t=10T/6$ to $2T$, the flow separation in the flow passages between guide vanes D and E and stay vanes C′ and D′ becomes increasingly stronger. Concurrently, the flow separation between guide vanes B and C shrinks and is limited near the vane trailing edge. Note that a "jet" occurs in the flow channel between guide vanes A and B.

The above results denote that both the rotating stall in the guide vane and stay vane regions shifts according to the runner rotation direction. Furthermore, the flow separation due to the rotating stall blocks the entire flow passage between two neighboring guide vanes and partly blocks the flow passage between two neighboring stay vanes. In the guide vane region, once the blockage is formed at a passage, a high-speed "jet" is formed in the last or next flow passage.

4.5 Lagrangian coherent structure

In this study, analysis of flow structure in the guide vane is also investigated by the Lagrangian coherent structure (LCS) to further reveal the propagation of rotating stall cells. For a time-dependent velocity field $\mathbf{v}(x, t)$, we define a trajectory $\mathbf{x}(t; t_0, \mathbf{x}_0)$ starting at point x_0 at time t_0. In a finite-time interval T_{LE}, initial point $\mathbf{x}(t_0; t_0, \mathbf{x}_0)$ moves to $\mathbf{x}(t_0+T_{\mathrm{LE}}; t_0, \mathbf{x}_0)$. The finite-time version of Cauchy-Green deformation tensor Δ [18] is defined as

$$\Delta_{t_0}^{T_{LE}}(\mathbf{x}_0)=\left[\frac{\partial \mathbf{x}(t_0+T_{LE};t_0,\mathbf{x}_0)}{\partial \mathbf{x}_0}\right]^{\mathrm{T}}\frac{\partial \mathbf{x}(t_0+T_{LE};t_0,\mathbf{x}_0)}{\partial \mathbf{x}_0}, \tag{11}$$

where $[\,]^{\mathrm{T}}$ is the transpose of the deformation gradient tensor. If $\lambda_{\max}(\Delta)$ is the maximum eigenvalue of Δ, then the largest finite-time Lyapunov exponent with a finite integration time T_{LE} is defined as

$$\sigma_{t_0}^{T_{LE}}(\mathbf{x}_0)=\frac{1}{|T_{LE}|}\ln\sqrt{\lambda_{\max}\left(\Delta_{t_0}^{T_{LE}}(\mathbf{x}_0)\right)}. \tag{12}$$

The Finite-time Lyapunov Exponent (FTLE) field is a scalar field that represents the maximum stretching rate for fluid particles. The ridge in the FTLE field is named as LCS.

Figure 11 shows the FTLE distributions of one typical runner revolution, which corresponds to the first revolution in Figure 10. Two types of LCSs, "LCS A" and "LCS B", can be observed. "LCS A" is located in the flow passage between guide vanes A and B and guide vanes C and D, representing the boundary of the vortex in the flow channels. It should be noted that those separation zones join together and block the flow passage between guide vanes A, B, and C. The formation of "LCS B" is induced by the guide vane geometric structure, as mentioned by Cheng et al. [19].

To present the flow separation phenomenon and transient process of the vortex dynamic, tracer particles are seeded normal to the guide vane pressure side. The tracer particles are initially located at $0.2c$ of guide vanes C and D as shown in Figure 12. Different colors represent the location of tracer particles at different time instants within one evolution. Figure 12(a) shows that the tracer particles near the suction side of guide vane C move upstream against the flow direction. This implies that the tracer particles are trapped to the vortex. The particles far away from the suction side move downstream following the main flow and mix at the trailing edge of guide vane D gradually. Figure 12(b) depicts the tracer particles moving downstream with the main flow. There is no flow separation in this region.

Figure 13 shows the FTLE distributions of the next typical runner revolution, which corresponds to the second periodic time in Figure 10. We can see two types of LCSs. "LSC A" shifts to guide vanes B, C, and D. The distribution of the

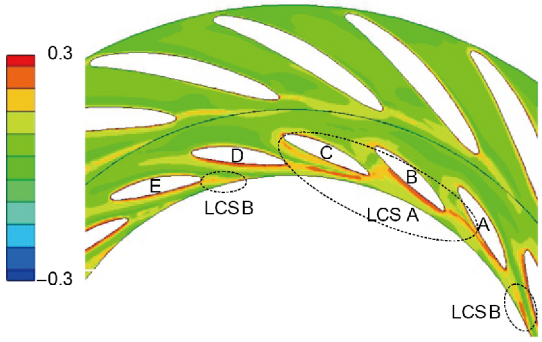

Figure 11 (Color online) FTLE distribution at one typical runner revolution (t_0, t_0+T), OP_1.

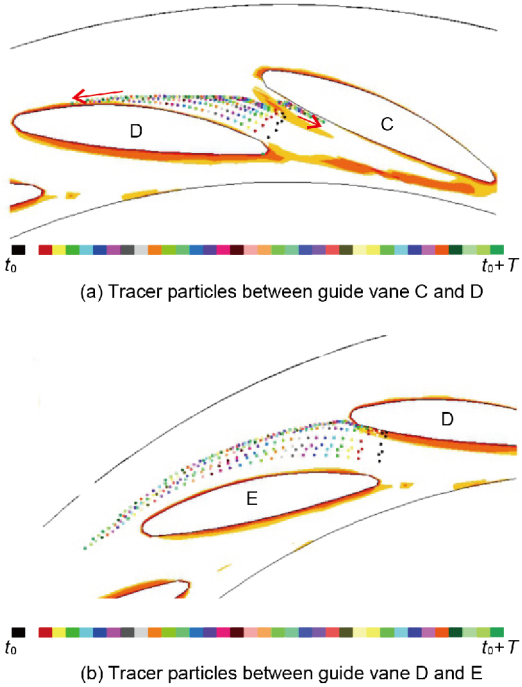

Figure 12 (Color online) Tracer particles at one typical runner revolution (t_0, t_0+T), OP_1.

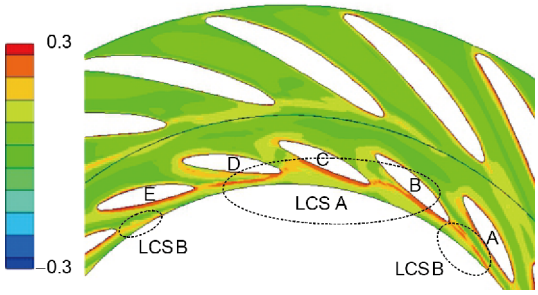

Figure 13 (Color online) FTLE distribution at one typical runner revolution (t_0+T, t_0+2T), OP_1.

LCSs in this periodic time is similar to those within the last revolution. Tracer particles are also seeded normal to the guide vane surface at 0.2c, and their trajectories are presented in Figure 14. Figure 14(a) shows that the tracer particles located at 0.2c of guide vane C are captured by the vortex and pushed toward the leading edge of the pressure side of guide vane D. This is consistent with the flow feature in Figure 10. Figure 14(b) displays the flow feature of tracer particles in the flow channel between guide vane D and E. The tracer particles near the suction side of guide vane D move upstream against the flow direction, which implies that the tracer particles are trapped to the vortex. The particles away from the suction side of guide vane D move downstream following the main flow and combine at the trailing edge of guide vane E gradually.

Figure 15 illustrates the behavior of rotating stall at drooping point OP_1. Once rotating stall is formed in the flow passage among guide vanes B, C, and D, the flow separates along the suction side of guide vanes B and C and the trailing edge of guide vane D. Reverse flow is observed near the suction side of the three guide vanes. The flow is blocked between guide vanes B and C. Concurrently, there is a leakage flowing to the leading edge of guide vane D. Owing to the blockage, a high-speed "jet" is formed near guide vane E. Unfavorable flows such as flow separation, reverse flow, leakage flow, and "jet" can cause significant hydraulic loss, and therefore, induce a performance breakdown at OP_1. There are three sets of rotating stall cells in the pump-turbine, whose positions move in the direction of the runner rotation.

4.6 Pressure fluctuations

Pressure fluctuations at time and frequency domains in the vaneless region at different operating points are shown in Figures 16 and 17. The pressure monitoring point is located in the vaneless region, as marked in Figure 9(a). From Figure 16(b), we can see the periodic pressure fluctuations at best efficiency point OP_3. However, at drooping point OP_1, a large pressure fluctuation with very low frequency is coupled with the periodic pressure fluctuation having relatively larger amplitude as shown in Figure 16(a). Figure 17 presents the

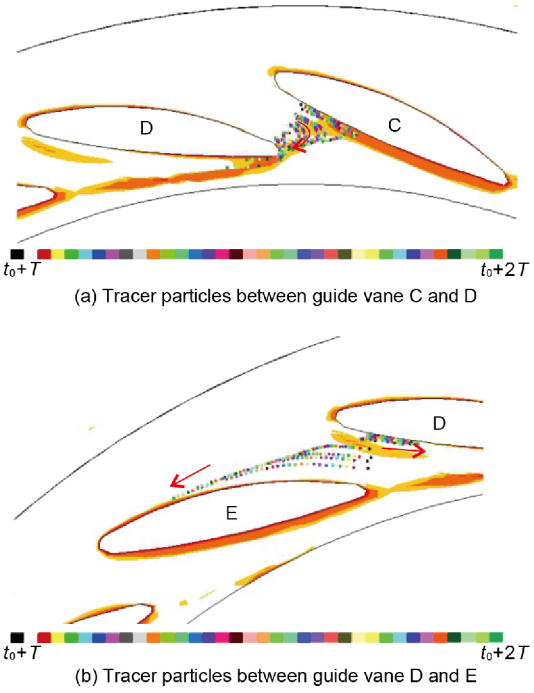

Figure 14 (Color online) Tracer particles at one typical runner revolution (t_0+T, t_0+2T), OP_1.

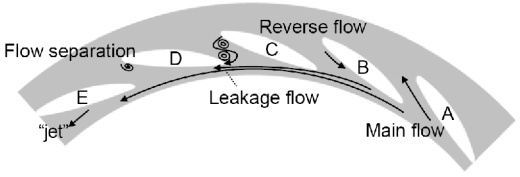

Figure 15 Illustration of the mechanism of rotating stall at OP_1.

pressure fluctuations by the fast Fourier transform (FFT) analysis. At best efficiency point OP_3, the dominant frequency of the pressure fluctuation is the blade passing frequency (7f_n) induced by the rotor-stator interaction, where f_n =18.33 Hz is the rotational frequency of the runner. At drooping point OP_1, though a pressure fluctuation component with blade passing frequency caused by runner rotating is still found, the dominant frequency of the pressure fluctuation is very low, i.e., 2.68 Hz (0.146f_n). According to the flow analysis, this pressure fluctuation with low frequency is induced by the rotating stall. Thus, the rotating stall is harmful for the safe operation of pumped storage power station because it induces both the performance breakdown and strong pressure fluctuation in the vaneless region in the pump-turbine at drooping point OP_1.

5 Conclusions

In this paper, unsteady numerical simulations are presented to depict the unstable flows near the positive slope conditions

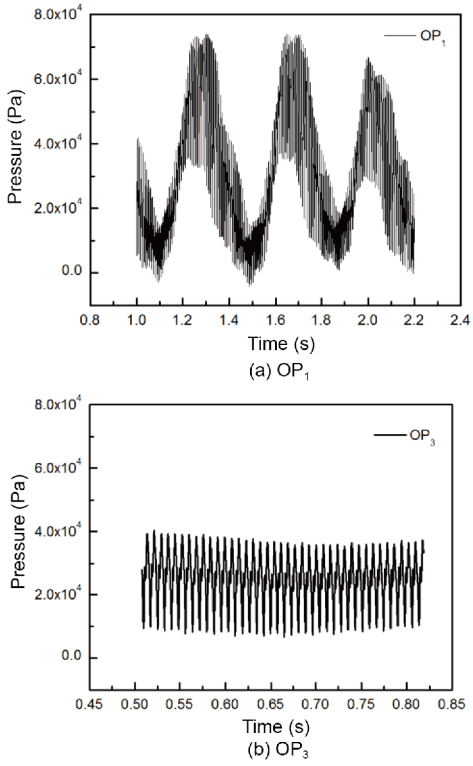

Figure 16 Pressure fluctuation at time domain in the vaneless region.

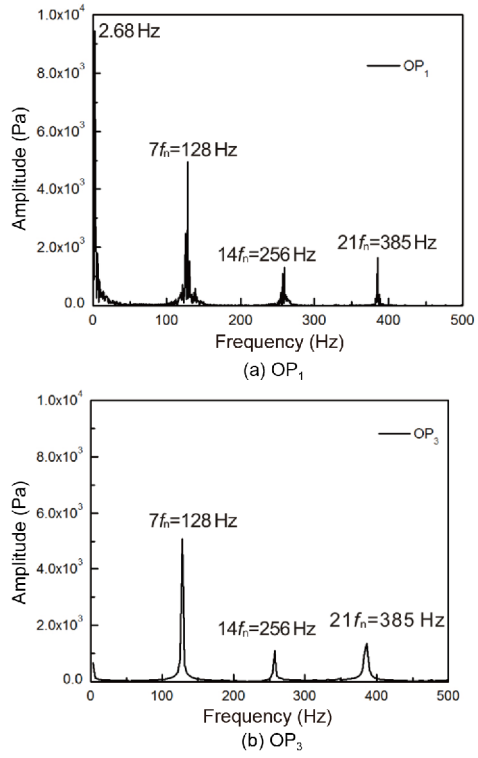

Figure 17 Pressure fluctuation at frequency domain in the vaneless region.

in a pump-turbine. The following conclusions can be drawn:

(1) It is confirmed that the present numerical method with the MPANS model predicts the positive slope characteristics in the pump-turbine at pump mode fairly well. The MPANS model yields more accurate numerical results compared with the conventional k-ω SST turbulence model.

(2) At drooping point OP_1, three sets of rotating stall cells are formed in the flow passages of both the guide vanes and stay vanes. In the guide vane region, the flow is completely shut off by the rotating stall, whereas in the stay vane region, the flow passage is partly blocked.

(3) The remarkable variation and significant values of AOA upstream the leading edge of guide vane contribute to the flow separation at the vane suction side and induce rotating stall in the flow passage at drooping point OP_1.

(4) The propagation of the rotating stall is depicted from both Eulerian and Lagrangian evidence. The rotating stall blocks the flow passage between two neighboring guide vanes and pushes the flow toward the leading edge of the subsequent guide vane. The rotating stall cell, which basically includes two separation zones, shifts along the rotational direction with a much lower frequency ($0.146f_n$) compared with the runner rotational frequency, f_n.

(5) Owing to the presence of rotating stall, performance breakdown and large amplitude pressure fluctuation occur in the vaneless region under the positive slope operation condition.

This work was supported by the National Natural Science Foundation of China (Grant No. 51536008), Beijing Natural Science Foundation (Grant No. 3182014), Science and Technology on Water Jet Propulsion Laboratory (Grant No. 6142223010316222300 4), and State Key Laboratory for Hydroscience and Engineering (Grant No. sklhse-2017-E-02).

1 Widmer C, Staubli T, Ledergerber N. Unstable characteristics and rotating stall in turbine brake operation of pump-turbines. J Fluids Eng, 2011, 133: 041101
2 Sinha M, Pinarbasi A, Katz J. The flow structure during onset and developed states of rotating stall within a vaned diffuser of a centrifugal pump. J Fluids Eng, 2001, 123: 490–499
3 Luo X W, Ji B, Tsujimoto Y. A review of cavitation in hydraulic machinery. J Hydrodyn Ser B, 2016, 28: 335–358
4 Ciocan G D, Kueny J L, Mesquita A A. Steady and unsteady flow pattern between stay and guide vanes in a pump-turbine. In: Cabrera E, Espert V, Martínez F, eds. Hydraul Machinery Cavitation. Dordrecht: Springer, 1996. 381–390
5 Ciocan G D, Kueny J L. Experimental analysis of the rotor-stator interaction in a pump-turbine. In: Proceedings of the Iahr Symposium. Yokohama, 2006. 216–226
6 Ran H J, Luo X W, Zhu L, et al. Experimental study of the pressure fluctuations in a pump turbine at large partial flow conditions. Chin J Mech Eng, 2012, 25: 1205–1209
7 Lu G C, Zuo Z G, Sun Y K, et al. Experimental evidence of cavitation influences on the positive slope on the pump performance curve of a low specific speed model pump-turbine. Renew Energy, 2017, 113: 1539–1550
8 Braun O, Kueny J L, Avellan F. Numerical analysis of flow phenomena related to the unstable energy-discharge characteristic of a pump-turbine in pump mode. In: ASME 2005 Fluids Engineering Division Summer Meeting. American Society of Mechanical Engineers, 2005. 1075–1080

9 Ran H J, Luo X W, Zhang Y, et al. Numerical simulation of the unsteady flow in a high-head pump turbine and the runner improvement. In: ASME 2008 Fluids Engineering Division Summer Meeting Collocated with the Heat Transfer, Energy Sustainability, and, Energy Nanotechnology Conferences, 2008. 1115–1123
10 Liu J T, Liu S H, Wu Y L, et al. Numerical investigation of the hump characteristic of a pump-turbine based on an improved cavitation model. Comput Fluids, 2012, 68: 105–111
11 Sun Y K, Zuo Z G, Liu S H, et al. Numerical study of pressure fluctuations in different guide vanes' opening angle in pump mode of a pump turbine. IOP Conf Ser-Earth Environ Sci, 2012, 15: 062037
12 Sun Y K, Zuo Z G, Liu S H, et al. Distribution of pressure fluctuations in a prototype pump turbine at pump mode. Adv Mech Eng, 2014, 6: 923937
13 Guo L, Liu J T, Wang L Q, et al. Pressure fluctuation propagation of a pump turbine at pump mode under low head condition. Sci China Tech Sci, 2014, 57: 811–818
14 Pacot O. Large Scale Computation of the rotating stall in a pump-turbine using an overset finite element large eddy simulation numerical code. Doctoral Dissertation. Switzerland: École polytechnique fédérale de Lausanne, 2014
15 Girimaji S S. Partially-averaged Navier-Stokes model for turbulence: A reynolds-averaged Navier-Stokes to direct numerical simulation bridging method. J Appl Mech, 2006, 73: 413–421
16 Girimaji S S. Abdol-Hamid K. Partially-averaged Navier Stokes model for turbulence: Implementation and validation. In: 43rd AIAA Aerospace Sciences Meeting and Exhibit-Meeting Papers. Reno, 2005
17 Huang R F, Luo X W, Ji B, et al. Turbulent flows over a backward facing step simulated using a modified partially averaged Navier-Stokes model. J Fluids Eng, 2017, 139: 044501
18 Shadden S C, Lekien F, Marsden J E. Definition and properties of Lagrangian coherent structures from finite-time Lyapunov exponents in two-dimensional aperiodic flows. Physica D, 2005, 212: 271–304
19 Cheng H Y, Long X P, Ji B, et al. Numerical investigation of unsteady cavitating turbulent flows around twisted hydrofoil from the Lagrangian viewpoint. J Hydrodyn Ser B, 2016, 28: 709–712